Small-Signal Modeling and Decoupling Control Method of Modular WPT Systems

Chen Zhu, *Student Member, IEEE*, and Wenxing Zhong, *Senior Member, IEEE*

***Abstract*—Modularization is an effective way to realize high-power wireless power transfer (WPT). A modular WPT system can be adaptive to multiple power levels by simply modifying the number of its modules. However, the cross couplings among different modules form complicated power transfer paths in the system and, consequently, the output of one module will be affected by the inputs of the other modules, and thereby it is difficult to achieve stable output regulation for each module by using the conventional negative-feedback control method. In this article, a decoupling control method is proposed to compensate for the adverse effect of the cross couplings among the modules, and, thereby, individual output control for each module can be realized. The small-signal model of the modular WPT system is derived to analyze the stability of the proposed decoupling control method. A 7-kW two-module WPT prototype is built for experimental verification.**

***Index Terms*—Decoupling control, modular wireless power transfer (WPT), small-signal model.**

I. Introduction

WIRELESS power transfer (WPT) can be used for charging industrial equipment, cellphones, electric vehicles (EVs), etc. [1], [2], [3]. Demand for developing fast wireless charging facilities as well as charging heavy-duty EVs encourages investigation of high power WPT. Efforts have been devoted to high-power stationary WPT with a power level up to 120 kW [4], [5], [6].

As the power level further increases, water-cooling systems become necessary for the windings due to concentrated power losses. Moreover, Litz wire with a large number of strands or parallel wires must be used to carry the large winding currents, which might lead to a lower quality factor of the windings and eventually a lower efficiency [7]. One of the promising solutions for high-power WPT is modularization. Modular WPT not only can address the above-mentioned issues but also has the advantages of scalable power level, minimal developing cost, module fault tolerance, etc. For example, the potential of using multiple modules to significantly attenuate the stray magnetic fields of a high-power WPT system is investigated in [8].

A modular WPT system contains multiple power transfer channels, each of which consists of a pair of transmitting and receiving coils [9]. This is the same as a polyphase WPT system [10], [11], [12], [13], [14], [15], [16]. The major difference between the modular system and the polyphase system is that the modular system can easily increase the number of modules and thus increase the power rating of the whole system. But the polyphase system is like a polyphase machine whose windings are designed as a whole and thereby the freedom of easily changing phases number is lost. Nevertheless, the modular WPT system has a similar issue as polyphase WPT systems, which is known as interphase cross coupling. Cross couplings in the context of this article are the couplings between two windings from two different modules, e.g., the coupling between two transmitting windings, the coupling between two receiving windings, or the coupling between the transmitting winding of one module and the receiving winding of a different module.

The cross couplings will result in unbalanced power among different modules [9], [17], [18], [19]. Thus, they cause degradation in the power transfer capability and efficiency of a modular WPT system. The following methods have been proposed to eliminate the effect of cross couplings.

1) The cross couplings of the windings at the same side (i.e., either the primary side or the secondary side) can be largely reduced by using the partially-overlapping structure as in a bipolar pad [20]. Similar structures are adopted in [21], [22], and [23]. However, overlapping structures are undesired in a modular WPT system with individual modules.
2) In [24] and [25] magnetic decoupled bipolar and unipolar coils overlapping each other are used to provide two-channel WPT. However, this structure is also not applicable to a modular WPT system.
3) In [26], a common impedance branch is added between two secondary-side resonator loops to cancel out the cross-coupling effect. However, two different loads are used in the system [26] to avoid a coupling caused by the same load.
4) In [27] and [28], the compensating capacitances are altered to cancel out the impedance due to the same-side cross couplings. The method is effective when the currents of the resonators have constant amplitude ratios and constant phase differences. However, this condition is normally not guaranteed in a modular WPT system.

Manuscript received 9 October 2022; revised 5 January 2023; accepted 5 February 2023. Date of publication 13 February 2023; date of current version 20 April 2023. This work was supported by the National Natural Science Foundation of China under Grant 51807174. This paper was presented in part at the IEEE Applied Power Electronics Conference and Exposition, New Orleans, LA, USA, March 2020. Recommended for publication by Associate Editor C. K. Tse. *(Corresponding author: Wenxing Zhong.)*

The authors are with the Institute of Power Electronics, Zhejiang University, Hangzhou 310027, China (e-mail: 11810044@zju.edu.cn; wxzhong@zju.edu.cn).

Color versions of one or more figures in this article are available at https://doi.org/10.1109/TPEL.2023.3244161.

Digital Object Identifier 10.1109/TPEL.2023.3244161

DQ decoupling control, based on the rotating coordinate transformation, has been widely adopted to realize the separate control of active and reactive currents in three-phase systems [29], [30]. Expanding the idea of counteracting the effect of coupled terms, a decoupling control for modular WPT systems is proposed in this article. The proposed decoupling control introduces an extra modification to the input voltage of each module which can cancel out the effect caused by the cross couplings. Thus, individual output control for each module is realized. The small-signal model of the modular WPT system is derived to analyze the stability of the proposed decoupling control method. Then, the performance of the proposed decoupling control is compared with the individual negative-feedback control through both simulation and experiments.

The rest of this article is organized as follows. In Section II, the small-signal model of the modular WPT system is derived. In Section III, the decoupling control method is proposed and its stability is analyzed based on the small-signal model. In Section IV, simulation verifications are provided. In Section V experimental results are given to verify the theoretical and simulation analyses. Finally, concluding remarks are provided in Section VI.

II. Small-Signal Modeling

A modular WPT system has multiple identical WPT modules. Each WPT module consists of one primary resonator, one secondary resonator, one primary-side power converter supplying the primary resonator, and one secondary-side converter rectifying the ac input from the secondary resonator to the dc output. The outputs of all WPT modules are connected in parallel to supply a load such as a battery. The schematic of a modular WPT system is shown in Fig. 1.

Following the generalized state-space averaging (GSSA) method described in [31] and [32], the GSSA model of a modular WPT system is given as follows:

First, the time-domain linear equations of Module j ($j = 1, 2, \ldots, n$) can be expressed as

$$
\begin{aligned}
&C_{Tj}\frac{du_{CTj}(t)}{dt} = i_{Tj}(t)\\
&C_{Rj}\frac{du_{CRj}(t)}{dt} = i_{Rj}(t)\\
&L_{Tj}\frac{di_{Tj}(t)}{dt} + \sum_{b=1}^{n} M_{TjRb}\frac{di_{Rb}(t)}{dt} + \sum_{c=1,c\neq j}^{n} M_{TjTc}\frac{di_{Tc}(t)}{dt}\\
&= u_j(t) - u_{CTj}(t)\\
&L_{Rj}\frac{di_{Rj}(t)}{dt} + \sum_{b=1}^{n} M_{TbRj}\frac{di_{Tb}(t)}{dt} + \sum_{c=1,c\neq j}^{n} M_{RjRc}\frac{di_{Rc}(t)}{dt}\\
&= u_{oj}(t) - u_{CRj}(t)\\
&L_{oj}\frac{di_{oj}(t)}{dt} = u_{Coj}(t) - U_o\\
&C_{oj}\frac{du_{Coj}(t)}{dt} = i_{Lj}(t) - i_{oj}(t)
\end{aligned}
\tag{1}
$$

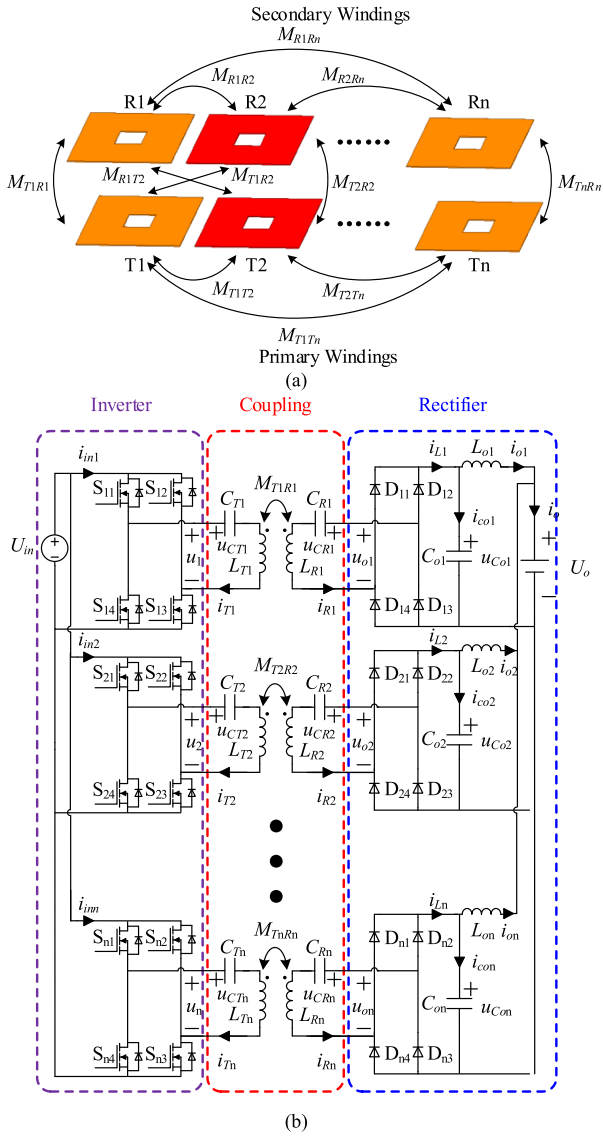

Fig. 1. n-module WPT system. (a) Schematic of the windings. (b) Circuit topology (cross mutual inductances not shown).

where subscript T and R denote the primary side and secondary side, respectively, L_{Tj} and L_{Rj} are the self-inductances, and C_{Tj} and C_{Rj} are the compensating capacitances of the transmitter and the receiver of Module j, respectively, L_{oj} and C_{oj} are the inductance and capacitance of the output filter, respectively, $M_{\gamma\delta}$ ($\gamma = T1, R1, \ldots, Tn, Rn$ and $\delta = T1, R1, \ldots, Tn, Rn$) is the mutual inductance between Resonator β and Resonator γ, $u_j(t)$ is the inverter output voltage, $u_{oj}(t)$ is the rectifier input voltage, $u_{Coj}(t)$ is the output filter capacitor voltage, $i_{Lj}(t)$ is the rectifier output current, $i_{oj}(t)$ is the battery charging current, $i_{Tj}(t)$ and $i_{Rj}(t)$ are the winding currents, $u_{CTj}(t)$ and $u_{CRj}(t)$ are the compensating capacitor voltages of the transmitter and the receiver, respectively, and U_o is the battery voltage.

For simplicity, the small-signal model of a two-module WPT system will be derived, which can be easily extended to an n-module system. Based on (1), the GSSA model of Module 1 in a two-module WPT system is derived as given in (2). In (2),

$\langle x\rangle_s$ and $\langle x\rangle_c$ are 1st Fourier coefficients for the Fourier series expansion of x [32].

$$\begin{cases} \frac{d\langle \boldsymbol{u_{C1}}\rangle}{dt} = \boldsymbol{C_1}\langle \boldsymbol{i_1}\rangle + \omega \boldsymbol{T_1}\langle \boldsymbol{u_{C1}}\rangle \\ \boldsymbol{M}\frac{d\langle \boldsymbol{i_{1s-2s}}\rangle}{dt} = \boldsymbol{T_2}\langle \boldsymbol{u_{1s}}\rangle + \omega \boldsymbol{M}\langle \boldsymbol{i_{1c-2c}}\rangle \\ \boldsymbol{M}\frac{d\langle \boldsymbol{i_{1c-2c}}\rangle}{dt} = \boldsymbol{T_2}\langle \boldsymbol{u_{1c}}\rangle - \omega \boldsymbol{M}\langle \boldsymbol{i_{1s-2s}}\rangle \\ L_{o1}\frac{di_{o1}}{dt} = u_{Co1} - U_o \\ C_{o1}\frac{du_{Co1}}{dt} = i_{L1} - i_{o1} \end{cases} \tag{2}$$

where

$$\langle \boldsymbol{u_{C1}}\rangle = [\langle u_{CT1}\rangle_s \langle u_{CT1}\rangle_c \langle u_{CR1}\rangle_s \langle u_{CR1}\rangle_c]^T$$

$$\langle \boldsymbol{i_1}\rangle = [\langle i_{T1}\rangle_s \langle i_{T1}\rangle_c \langle i_{R1}\rangle_s \langle i_{R1}\rangle_c]^T$$

$$\langle \boldsymbol{i_{1s-2s}}\rangle = [\langle i_{T1}\rangle_s \langle i_{R1}\rangle_s \langle i_{T2}\rangle_s \langle i_{R2}\rangle_s]^T$$

$$\langle \boldsymbol{i_{1c-2c}}\rangle = [\langle i_{T1}\rangle_c \langle i_{R1}\rangle_c \langle i_{T2}\rangle_c \langle i_{R2}\rangle_c]^T$$

$$\langle \boldsymbol{u_{1s}}\rangle = [\langle u_1\rangle_s \langle u_{CT1}\rangle_s \langle u_{o1}\rangle_s \langle u_{CR1}\rangle_s]^T$$

$$\langle \boldsymbol{u_{1c}}\rangle = [\langle u_1\rangle_c \langle u_{CT1}\rangle_c \langle u_{o1}\rangle_c \langle u_{CR1}\rangle_c]^T$$

$$\boldsymbol{C_1} = \begin{bmatrix} \frac{1}{C_{T1}} & 0 & 0 & 0 \\ 0 & \frac{1}{C_{T1}} & 0 & 0 \\ 0 & 0 & \frac{1}{C_{R1}} & 0 \\ 0 & 0 & 0 & \frac{1}{C_{R1}} \end{bmatrix}$$

$$\boldsymbol{T_1} = \begin{bmatrix} 0 & 1 & 0 & 0 \\ -1 & 0 & 0 & 0 \\ 0 & 0 & 0 & 1 \\ 0 & 0 & -1 & 0 \end{bmatrix}$$

$$\boldsymbol{T_2} = \begin{bmatrix} 1 & -1 & 0 & 0 \\ 0 & 0 & 1 & -1 \end{bmatrix}$$

$$\boldsymbol{M} = \begin{bmatrix} L_{T1} & M_{T1R1} & M_{T1T2} & M_{T1R2} \\ M_{T1R1} & L_{R1} & M_{R1T2} & M_{R1R2} \end{bmatrix}.$$

The extended describing function (EDF) method is normally used to deal with the nonlinear characteristics of the converters [33], [34]. Following the EDF method, the fundamental component of the input voltage of Module 1 $u_1(t)$ is given by

$$u_1(t) = \frac{4}{\pi}U_{\text{in}}\sin\left(\frac{\alpha_1}{2}\right)\sin(\omega t + \theta_1) \tag{3}$$

where α_1 is the phase shift angle of the inverter legs of Module 1, and θ_1 the phase angle of the fundamental component of the inverter output voltage of Module 1, which can be set to 0 as a phase reference. Using θ_{S11} and θ_{S21} to represent the phase of the switching signal of S_{11} and S_{21} in Fig. 1(b), the switching sequence chart of the two-module WPT system can be determined, as shown in Fig. 2.

Then, (3) can be rewritten as

$$\begin{cases} \langle u_1\rangle_s = \frac{4}{\pi}U_{\text{in}}\sin\left(\frac{\alpha_1}{2}\right)\cos\theta_1 \\ \langle u_1\rangle_c = \frac{4}{\pi}U_{\text{in}}\sin\left(\frac{\alpha_1}{2}\right)\sin\theta_1. \end{cases} \tag{4}$$

The nonlinear terms of the rectifier, including $i_{L1}(t)$ and $u_{o1}(t)$, are given by

$$\begin{cases} i_{L1}(t) = |i_{R1}(t)| \\ u_{o1}(t) = u_{Co1}(t)\text{sgn}\left(i_{R1}(t)\right) \end{cases} \tag{5}$$

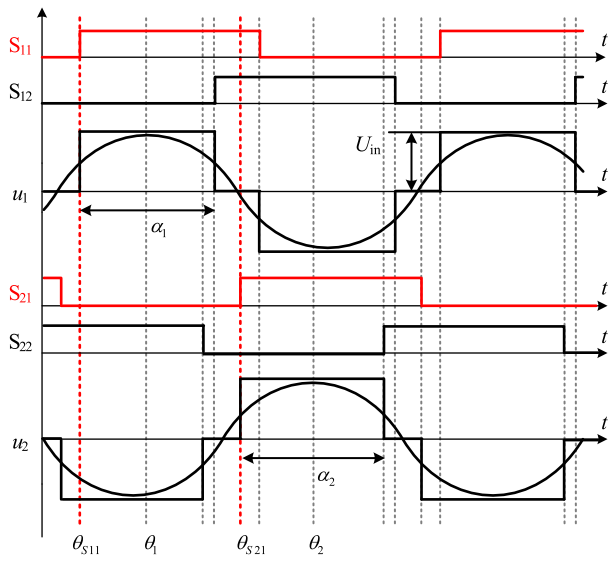

Fig. 2. Inverter switching signal and inverter output voltage of a two-module WPT system.

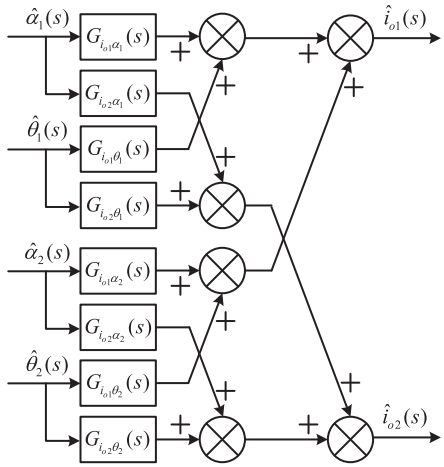

Fig. 3. Small-signal model of the two-module WPT system.

where sgn represents the sign function and $i_{R1}(t)$ can be expressed as

$$\begin{aligned} i_{R1}(t) &= \langle i_{R1}\rangle_s \sin\omega t + \langle i_{R1}\rangle_c \cos\omega t \\ &= \langle i_{R1}\rangle_p \frac{\langle i_{R1}\rangle_s}{\langle i_{R1}\rangle_p}\sin\omega t + \langle i_{R1}\rangle_p \frac{\langle i_{R1}\rangle_c}{\langle i_{R1}\rangle_p}\cos\omega t \\ &= \langle i_{R1}\rangle_p \sin(\omega t + \beta) \end{aligned} \tag{6}$$

where

$$\langle i_{R1}\rangle_p = \sqrt{\langle i_{R1}\rangle_s^2 + \langle i_{R1}\rangle_c^2}$$

$$\sin\beta = \frac{\langle i_{R1}\rangle_c}{\langle i_{R1}\rangle_p}$$

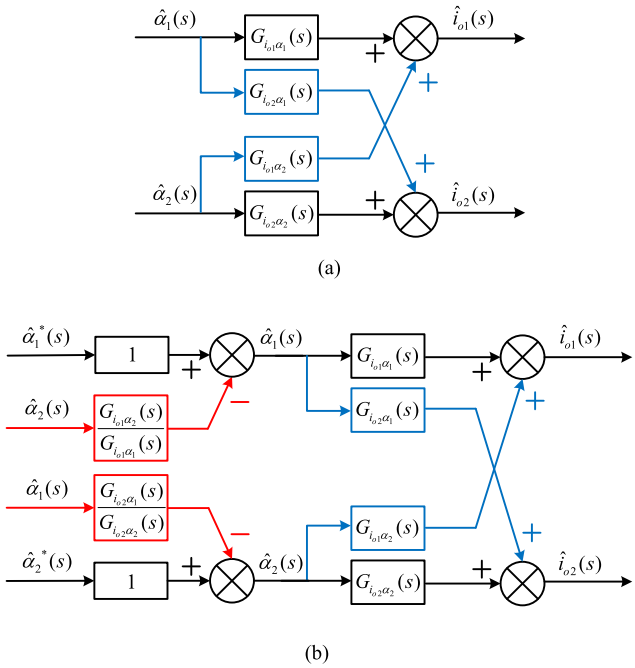

Fig. 4. Small-signal model of the two-module WPT system. (a) Before modifying the phase shift angle. (b) After modifying the phase shift angle.

$$\cos\beta = \frac{\langle i_{R1}\rangle_s}{\langle i_{R1}\rangle_p}.$$

Here, only the fundamental frequency is considered. Therefore

$$\begin{aligned} \langle |i_{R1}| \rangle &= \langle i_{R1}\rangle_p \\ \operatorname{sgn}\left(i_{R1}(t)\right) &= \langle \operatorname{sgn}(i_{R1})\rangle_s \sin\omega t + \langle \operatorname{sgn}(i_{R1})\rangle_c \cos\omega t \end{aligned} \quad (7)$$

where

$$\langle \operatorname{sgn}(i_{R1})\rangle_s = \frac{\omega}{\pi}\int_0^{\frac{2\pi}{\omega}} \operatorname{sgn}\left(i_{R1}(t)\right)\sin\omega t\cdot dt = \frac{4}{\pi}\cos\beta$$

$$\langle \operatorname{sgn}(i_{R1})\rangle_c = \frac{\omega}{\pi}\int_0^{\frac{2\pi}{\omega}} \operatorname{sgn}\left(i_{R1}(t)\right)\cos\omega t\cdot dt = \frac{4}{\pi}\sin\beta.$$

According to (6) and (7), (5) can be rewritten as

$$\begin{cases} i_{L1} = \frac{2}{\pi}\langle |i_{R1}| \rangle \\ u_{o1}(t) = \frac{4}{\pi}\frac{\langle i_{R1}\rangle_s}{\langle i_{R1}\rangle_p} u_{Co1}(t)\sin\omega t + \frac{4}{\pi}\frac{\langle i_{R1}\rangle_c}{\langle i_{R1}\rangle_p} u_{Co1}(t)\cos\omega t. \end{cases} \quad (8)$$

The large signal model of Module 1 in the two-module WPT system is then given by (2), (4), and (8).

The state-space equation of the two-module system is given by

$$\begin{cases} \dot{\boldsymbol{x}} = \boldsymbol{A}\boldsymbol{x} + \boldsymbol{B}\boldsymbol{u} \\ \boldsymbol{y} = \boldsymbol{C}\boldsymbol{x} \end{cases} \quad (9)$$

where $\boldsymbol{x}$ is the state variable vector containing the sine and cosine coefficients of currents and voltages, which is given by

$$\begin{aligned} \boldsymbol{x} = \{&\langle i_{T1}\rangle_s, \langle i_{T1}\rangle_c, \langle i_{R1}\rangle_s, \langle i_{R1}\rangle_c, \langle u_{CT1}\rangle_s, \langle u_{CT1}\rangle_c, \langle u_{CR1}\rangle_s \\ &\langle u_{CR1}\rangle_c, u_{Co1}, i_{o1}, \langle i_{T2}\rangle_s, \langle i_{T2}\rangle_c, \langle i_{R2}\rangle_s, \langle i_{R2}\rangle_c, \langle u_{CT2}\rangle_s \\ &\langle u_{CT2}\rangle_c, \langle u_{CR2}\rangle_s, \langle u_{CR2}\rangle_c, u_{Co2}, i_{o2}\}. \end{aligned}$$

where $\boldsymbol{u}$ and $\boldsymbol{y}$ are the input and output vectors, respectively, given by

$$\begin{aligned} \boldsymbol{u} &= \{\alpha_1, \theta_1, \alpha_2, \theta_2\} \\ \boldsymbol{y} &= \{i_{o1}, i_{o2}\}. \end{aligned}$$

$\boldsymbol{A}$, $\boldsymbol{B}$, and $\boldsymbol{C}$ are matrixes that can be obtained from the following equation:

$$\begin{cases} \frac{d\langle \hat{\boldsymbol{u}}_{\boldsymbol{C1}}\rangle}{dt} = \boldsymbol{C_1}\left\langle \hat{\boldsymbol{i}}_{\boldsymbol{1}}\right\rangle + \omega \boldsymbol{T_1}\langle \hat{\boldsymbol{u}}_{\boldsymbol{C1}}\rangle \\ \boldsymbol{M}\frac{d\left\langle \hat{\boldsymbol{i}}_{\boldsymbol{1s-2s}}\right\rangle}{dt} = \frac{2}{\pi}U_{in}\boldsymbol{H_1}\begin{bmatrix}\hat{\alpha}_1 & \hat{\theta}_1\end{bmatrix}^T \\ -\boldsymbol{V}_1[\langle \hat{u}_{CT1}\rangle_s \langle \hat{u}_{CR1}\rangle_s \hat{u}_{Co1}]^T \\ +\boldsymbol{M}\boldsymbol{D_1}\begin{bmatrix}\langle \hat{i}_{R1}\rangle_s & \langle \hat{i}_{R1}\rangle_c\end{bmatrix}^T + \omega \boldsymbol{M}\left\langle \hat{\boldsymbol{i}}_{\boldsymbol{1c-2c}}\right\rangle \\ \boldsymbol{M}\frac{d\left\langle \hat{\boldsymbol{i}}_{\boldsymbol{1c-2c}}\right\rangle}{dt} = \frac{2}{\pi}U_{in}\boldsymbol{H_2}\begin{bmatrix}\hat{\alpha}_1 & \hat{\theta}_1\end{bmatrix}^T \\ -\boldsymbol{V_2}[\langle \hat{u}_{CT1}\rangle_c \langle \hat{u}_{CR1}\rangle_c \hat{u}_{Co1}]^T \\ -\boldsymbol{M}\boldsymbol{D_2}\begin{bmatrix}\langle \hat{i}_{R1}\rangle_s & \langle \hat{i}_{R1}\rangle_c\end{bmatrix}^T - \omega \boldsymbol{M}\left\langle \hat{\boldsymbol{i}}_{\boldsymbol{1s-2s}}\right\rangle \\ L_{o1}\frac{d\hat{i}_{o1}}{dt} = \hat{u}_{Co1} \\ C_{o1}\frac{d\hat{u}_{Co1}}{dt} = \frac{2}{\pi}\frac{I_{R1s}\langle \hat{i}_{R1}\rangle_s + I_{R1c}\langle \hat{i}_{R1}\rangle_c}{\sqrt{I_{R1s}^2 + I_{R1c}^2}} - \hat{i}_{o1} \end{cases} \quad (10)$$

where

$$\langle \hat{\boldsymbol{u}}_{\boldsymbol{C1}}\rangle = \begin{bmatrix}\langle \hat{u}_{CT1}\rangle_s & \langle \hat{u}_{CT1}\rangle_c & \langle \hat{u}_{CR1}\rangle_s & \langle \hat{u}_{CR1}\rangle_c\end{bmatrix}^T$$

$$\left\langle \hat{\boldsymbol{i}}_{\boldsymbol{1}}\right\rangle = \begin{bmatrix}\langle \hat{i}_{T1}\rangle_s & \langle \hat{i}_{T1}\rangle_c & \langle \hat{i}_{R1}\rangle_s & \langle \hat{i}_{R1}\rangle_c\end{bmatrix}^T$$

$$\left\langle \hat{\boldsymbol{i}}_{\boldsymbol{1s-2s}}\right\rangle = \begin{bmatrix}\langle \hat{i}_{T1}\rangle_s & \langle \hat{i}_{R1}\rangle_s & \langle \hat{i}_{T2}\rangle_s & \langle \hat{i}_{R2}\rangle_s\end{bmatrix}^T$$

$$\left\langle \hat{\boldsymbol{i}}_{\boldsymbol{1c-2c}}\right\rangle = \begin{bmatrix}\langle \hat{i}_{T1}\rangle_c & \langle \hat{i}_{R1}\rangle_c & \langle \hat{i}_{T2}\rangle_c & \langle \hat{i}_{R2}\rangle_c\end{bmatrix}^T$$

$$\boldsymbol{H_1} = \begin{bmatrix}\cos\left(\frac{A_1}{2}\right)\cos\boldsymbol{\Theta}_1 & -2\sin\left(\frac{A_1}{2}\right)\sin\boldsymbol{\Theta}_1 \\ 0 & 0\end{bmatrix}$$

$$\boldsymbol{H_2} = \begin{bmatrix}\cos\left(\frac{A_1}{2}\right)\sin\boldsymbol{\Theta}_1 & 2\sin\left(\frac{A_1}{2}\right)\cos\boldsymbol{\Theta}_1 \\ 0 & 0\end{bmatrix}$$

$$\boldsymbol{V_1} = \begin{bmatrix}1 & 0 & 0 \\ 0 & 1 & \frac{-4I_{R1s}}{\pi\sqrt{I_{R1s}^2 + I_{R1c}^2}}\end{bmatrix}$$

$$\boldsymbol{V_2} = \begin{bmatrix}1 & 0 & 0 \\ 0 & 1 & \frac{4I_{R1c}}{\pi\sqrt{I_{R1s}^2 + I_{R1c}^2}}\end{bmatrix}^T$$

$$\boldsymbol{D_1} = \begin{bmatrix}0 & 0 \\ \frac{4I_{R1c}^2 U_{Co1}}{\pi\left(I_{R1s}^2 + I_{R1c}^2\right)^{3/2}} & -\frac{4\omega I_{R1s} I_{R1c} U_{Co1}}{\pi\left(I_{R1s}^2 + I_{R1c}^2\right)^{3/2}}\end{bmatrix}$$

$$\boldsymbol{D_2} = \begin{bmatrix}0 & 0 \\ -\frac{4\omega I_{R1s} I_{R1c} U_{Co1}}{\pi\left(I_{R1s}^2 + I_{R1c}^2\right)^{3/2}} & \frac{4I_{R1s}^2 U_{Co1}}{\pi\left(I_{R1s}^2 + I_{R1c}^2\right)^{3/2}}\end{bmatrix}.$$

By adding a perturbation to a steady-state operating point, the small-signal model of the two-module WPT system can be derived as (10), where A_1, A_2, and Θ_1, Θ_2 are the steady-state values of α_1, α_2, and θ_1, θ_2, respectively. The transfer function

matrix can be expressed as

$$\begin{bmatrix}\hat{i}_{o1}(s)\\ \hat{i}_{o2}(s)\end{bmatrix}=\begin{bmatrix}G_{i_{o1}\alpha_1}(s) & G_{i_{o1}\theta_1}(s) & G_{i_{o1}\alpha_2}(s) & G_{i_{o1}\theta_2}(s)\\ G_{i_{o2}\alpha_1}(s) & G_{i_{o2}\theta_1}(s) & G_{i_{o2}\alpha_2}(s) & G_{i_{o2}\theta_2}(s)\end{bmatrix}\begin{bmatrix}\hat{\alpha}_1(s)\\ \hat{\theta}_1(s)\\ \hat{\alpha}_2(s)\\ \hat{\theta}_2(s)\end{bmatrix} \tag{11}$$

where

$$\begin{bmatrix}G_{i_{o1}\alpha_1}(s) & G_{i_{o1}\theta_1}(s) & G_{i_{o1}\alpha_2}(s) & G_{i_{o1}\theta_2}(s)\\ G_{i_{o2}\alpha_1}(s) & G_{i_{o2}\theta_1}(s) & G_{i_{o2}\alpha_2}(s) & G_{i_{o2}\theta_2}(s)\end{bmatrix}=\boldsymbol{C}(s\boldsymbol{I}-\boldsymbol{A})^{-1}\boldsymbol{B}.$$

According to (11), the block diagram of the small-signal model of the two-module WPT system is given in Fig. 3.

It is obvious that the output currents are determined by all the input terms of the two modules. To realize individual output control, the interactions between two modules should be counteracted.

III. Decoupling Control Method

A. Decoupling Control By Altering Input Voltages

In the rest of this article, the phase angles of the input voltages are assumed given and unchanged to simply the control scheme of the system. Therefore, only the phase shift angles of the inverters are the control variables.

According to (11), adjusting the phase shift angle of one module will also affect the output current of the other module. One solution is to alter the phase shift angle of each module in a way that the influence of the other module can be eliminated. More specifically, the phase shift angle of each module can be divided into two components, one is called the *decoupled phase shift angle* (denoted as $\hat{\alpha}_i^*$, $i=1,2$) corresponding to the output control of each module regardless of the interactions and it can be calculated in real-time with a conventional negative-feedback controller; the other component cancels out the effect of all interactions on the output in real-time. The concept is illustrated in Fig. 4, where the blue blocks are the interactions between two modules due to the cross couplings. To cancel out these interactions, the red blocks representing the decoupling components are added in Fig. 4(b).

Based on Fig. 4, the actual phase shift angles which are applied to the inverters are modified as

$$\hat{\alpha}_1(s)=\hat{\alpha}_1^*(s)-\frac{G_{i_{o1}\alpha_2}(s)}{G_{i_{o1}\alpha_1}(s)}\hat{\alpha}_2(s) \tag{12}$$

$$\hat{\alpha}_2(s)=\hat{\alpha}_2^*(s)-\frac{G_{i_{o2}\alpha_1}(s)}{G_{i_{o2}\alpha_2}(s)}\hat{\alpha}_1(s) \tag{13}$$

where $\hat{\alpha}_1^*(s)$ and $\hat{\alpha}_2^*(s)$ are the decoupled phase shift angles. The latter terms in (12) and (13) exactly cancel out the interactions between the two modules. Because $\hat{\alpha}_1^*(s)$ and $\hat{\alpha}_2^*(s)$ are expected to be calculated by the controller (e.g., PI), the actual phase shift angles of the inverters, i.e., $\hat{\alpha}_1(s)$ and $\hat{\alpha}_2(s)$, should be expressed as functions of $\hat{\alpha}_1^*(s)$ and $\hat{\alpha}_2^*(s)$. By solving (12) and (13), $\hat{\alpha}_1(s)$ and $\hat{\alpha}_2(s)$ are given by

$$\begin{cases}\hat{\alpha}_1(s)=G(s)\left(\hat{\alpha}_1^*(s)-\frac{G_{i_{o1}\alpha_2}(s)}{G_{i_{o1}\alpha_1}(s)}\hat{\alpha}_2^*(s)\right)\\ \hat{\alpha}_2(s)=G(s)\left(\hat{\alpha}_2^*(s)-\frac{G_{i_{o2}\alpha_1}(s)}{G_{i_{o2}\alpha_2}(s)}\hat{\alpha}_1^*(s)\right)\end{cases} \tag{14}$$

TABLE I
Parameters of the Steady-State Operating Point

Parameters	Values
I_{1Ts}	11.1 A
I_{1Tc}	3.2 A
I_{1Rs}	-5.2 A
I_{1Rc}	-12.0 A
U_{C1Ts}	356 V
U_{C1Tc}	-2249 V
U_{C1Rs}	-2297 V
U_{C1Rc}	1171 V
U_{Co1}	330 V
I_{o1}	11.8 A
I_{2Ts}	-11.1 A
I_{2Tc}	-3.2 A
I_{2Rs}	5.2 A
I_{2Rc}	12.0 A
U_{C2Ts}	-356 V
U_{C2Tc}	2249 V
U_{C2Rs}	2297 V
U_{C2Rc}	-1144 V
U_{Co1}	330 V
I_{o2}	11.8 A

where $G(s)$ is given by

$$G(s)=\frac{G_{i_{o1}\alpha_1}(s)G_{i_{o2}\alpha_2}(s)}{G_{i_{o1}\alpha_1}(s)G_{i_{o2}\alpha_2}(s)-G_{i_{o1}\alpha_2}(s)G_{i_{o2}\alpha_1}(s)}.$$

By substituting (14) into (11), the output currents now become

$$\begin{cases}\hat{i}_{o1}(s)=G(s)\left(G_{i_{o1}\alpha_1}(s)-\frac{G_{i_{o1}\alpha_2}(s)G_{i_{o2}\alpha_1}(s)}{G_{i_{o2}\alpha_2}(s)}\right)\hat{\alpha}_1^*(s)\\ \hat{i}_{o2}(s)=G(s)\left(G_{i_{o2}\alpha_2}(s)-\frac{G_{i_{o1}\alpha_2}(s)G_{i_{o2}\alpha_1}(s)}{G_{i_{o1}\alpha_1}(s)}\right)\hat{\alpha}_2^*(s).\end{cases} \tag{15}$$

Thereby, the output of each module can be individually adjusted according to (15) after adding the decoupling terms.

To simplify the calculations, $G(s)$ in (15) can be eliminated by changing the actual input phase shift angles to

$$\begin{cases}\hat{\alpha}_1(s)=\hat{\alpha}_1^*(s)-\frac{G_{i_{o1}\alpha_2}(s)}{G_{i_{o1}\alpha_1}(s)}\hat{\alpha}_2^*(s)\\ \hat{\alpha}_2(s)=\hat{\alpha}_2^*(s)-\frac{G_{i_{o2}\alpha_1}(s)}{G_{i_{o2}\alpha_2}(s)}\hat{\alpha}_1^*(s).\end{cases} \tag{16}$$

Under the condition of (16), the output currents become

$$\begin{cases}\hat{i}_{o1}(s)=\left(G_{i_{o1}\alpha_1}(s)-\frac{G_{i_{o1}\alpha_2}(s)G_{i_{o2}\alpha_1}(s)}{G_{i_{o2}\alpha_2}(s)}\right)\hat{\alpha}_1^*(s)\\ \hat{i}_{o2}(s)=\left(G_{i_{o2}\alpha_2}(s)-\frac{G_{i_{o1}\alpha_2}(s)G_{i_{o2}\alpha_1}(s)}{G_{i_{o1}\alpha_1}(s)}\right)\hat{\alpha}_2^*(s).\end{cases} \tag{17}$$

According to (17), the output current of each module is only dependent on the corresponding decoupled input phase shift angle, as shown in Fig. 5.

Similarly, the decoupling method can be extended to an n-module system described with (18) and the input phase shift angles of the n-module WPT system are modified to (19) for

TABLE II
PARAMTERS OF THE WINDINGS

Parameters	Values
Coil outer diameter	350 mm
Coil inner diameter	90 mm
Litz line parameter	0.1×900
Turns of transmitting coil	30
Turns of receiving coil	30
Spacing @coil and core	3 mm
Core size	370 mm×370 mm×5 mm
Spacing @core and shielding layer	15 mm
Shielding layer size	350 mm×350 mm×1 mm
Air gap	22.5 cm

TABLE III
PARAMETERS OF THE TWO-MODULE WPT SYSTEM AT THE ALIGNED POSITION

Parameters	Values
R_{AC}	0.189 Ω
L_{*T} 、L_{*R}	369.9 μH
M_{1T1R}	49.5 μH
M_{1T2T}	-29.2 μH
M_{1T2R}	-11.8 μH
M_{1R2T}	-11.9 μH
M_{1R2R}	-29.1 μH
M_{2T2R}	49.5 μH
C_{o1}	400 μF
L_{o1}	100 nH
θ_1	0°
θ_2	180°
K_p	0.001
K_i	10

TABLE IV
PARAMETERS OF THE THREE-MODULE WPT SYSTEM AT THE ALIGNED POSITION

Parameters	Values	Parameters	Values
R_{AC}	0.205 Ω	L_{*T} 、L_{*R}	371.7 μH
M_{1T1R} 、M_{3T3R}	48.8 μH	M_{2T2R}	52.6 μH
M_{1R2T} 、M_{2R3T}	-9.3 μH	M_{1T2T} 、M_{2T3T}	-26.1 μH
M_{1R2R} 、M_{2R3R}	-26.0 μH	M_{1T2R} 、M_{2T3R}	-9.2 μH
M_{1T3T} 、M_{1R3R}	-10.7 μH	M_{1T3R} 、M_{1R3T}	-9.1 μH
θ_1	0°	θ_2	135°
θ_3	0°	K_p	0.0001
K_i	10		

TABLE V
PARAMETERS OF THE FOUR-MODULE WPT SYSTEM AT THE ALIGNED POSITION

Parameters	Values	Parameters	Values
R_{AC}	0.232 Ω	L_{*T} 、L_{*R}	375.3 μH
M_{*T*R}	54.5 μH	M_{*T*T} 、M_{*R*R}	-21.5 μH
M_{1T3T} 、M_{1R3R}	-10.2 μH	M_{2T4T} 、M_{2R4R}	-10.1 μH
M_{1T2R} 、M_{3R4T}	-6.7 μH	M_{1R2T} 、M_{3T4R}	-6.7 μH
M_{1T4R} 、M_{1R4T}	-6.7 μH	M_{2T3R} 、M_{2R3T}	-6.6 μH
M_{1T3R} 、M_{2R4T}	-8.3 μH	M_{1R3T} 、M_{2T4R}	-8.3 μH
θ_1	0°	θ_2	180°
θ_3	180°	θ_4	0°
K_p	0.00001	K_i	10

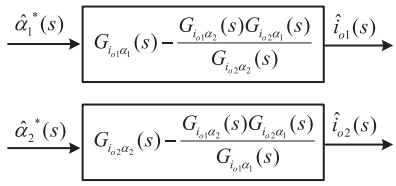

Fig. 5. Decoupled model of the two-module WPT system.

decoupling control.

$$\begin{bmatrix}\hat{i}_{o1}\\ \vdots\\ \hat{i}_{on}\end{bmatrix} = \begin{bmatrix} G_{i_{o1}\alpha_1}(s) & G_{i_{o1}\theta_1}(s) & \cdots & G_{i_{o1}\alpha_n}(s) & G_{i_{o1}\theta_n}(s)\\ \vdots & \vdots & \ddots & \vdots & \vdots\\ G_{i_{on}\alpha_1}(s) & G_{i_{on}\theta_1}(s) & \cdots & G_{i_{on}\alpha_n}(s) & G_{i_{on}\theta_n}(s)\end{bmatrix} \times \begin{bmatrix}\hat{\alpha}_1\\ \hat{\theta}_1\\ \vdots\\ \hat{\alpha}_n\\ \hat{\theta}_n\end{bmatrix} \tag{18}$$

$$\begin{cases}\hat{\alpha}_1(s)=\hat{\alpha}_1^*(s)-\frac{G_{i_{o1}\alpha_2}(s)}{G_{i_{o1}\alpha_1}(s)}\hat{\alpha}_2(s)-\cdots-\frac{G_{i_{o1}\alpha_n}(s)}{G_{i_{o1}\alpha_1}(s)}\hat{\alpha}_n(s)\\ \vdots\\ \hat{\alpha}_n(s)=\hat{\alpha}_n^*(s)-\frac{G_{i_{\mathrm{ON}}\alpha_1}(s)}{G_{i_{\mathrm{ON}}\alpha_n}(s)}\hat{\alpha}_1(s)-\cdots-\frac{G_{i_{\mathrm{ON}}\alpha_{n-1}}(s)}{G_{i_{\mathrm{ON}}\alpha_n}(s)}\hat{\alpha}_{n-1}(s).\end{cases} \tag{19}$$

B. Implementation of Decoupling Control of Two-Module WPT System

According to (16) and Fig. 3, the decoupling control block diagram is given in Fig. 6. In the control block diagram, the output current of each module, i.e., $\hat{i}_{oi}(s)(i=1,2)$, is compared with the reference value $\hat{i}_{\mathrm{ref}-oi}(s)$. The error is then used to calculate the decoupled phase shift angle $\hat{\alpha}_i^*(s)$ with a conventional PI block. A delay $e^{-\tau s}$ might be introduced, e.g., by wireless communication. Then the decoupled phase shift angles are utilized to calculate the actual input phase shift angles of the inverters. The actual input phase shift angles are calculated according to (16) of Section III-A.

The RMS value of the fundamental component of the inverter output voltage is [35]

$$U_i=\frac{4}{\pi}U_{\mathrm{in}}\sin\left(\frac{\alpha_i(t)}{2}\right) \tag{20}$$

where U_i is the amplitude of the inverter output voltage, U_{in} is the dc input voltage, and $\alpha_i(t)$ is the phase shift angle of two inverter legs.

Therefore, once the actual phase shift angles are determined via (16), the amplitudes of the input voltages can be derived with (20). On the other hand, the phase difference between $u_1(t)$ and $u_2(t)$, i.e., $\theta_2(t)-\theta_1(t)$, determines the switching timing of the

TABLE VI
SIMULATION RESULTS

	two-module system	three-module system	four-module system
Conventional individual negative-feedback control (I_{o1} and I_{o2} are average values)	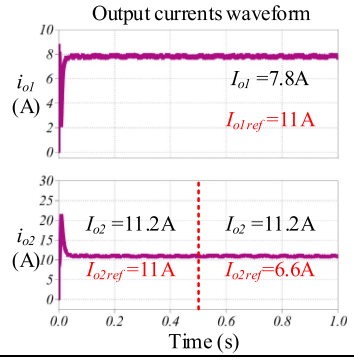	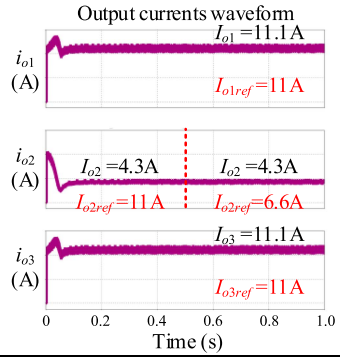	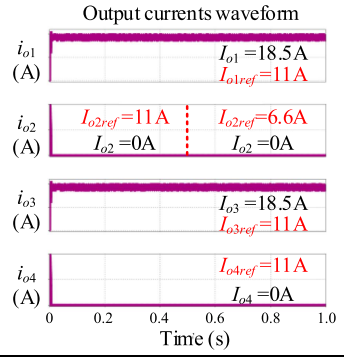
Decoupling control (I_{o1} and I_{o2} are average values)	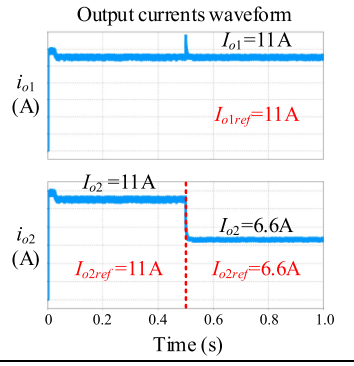	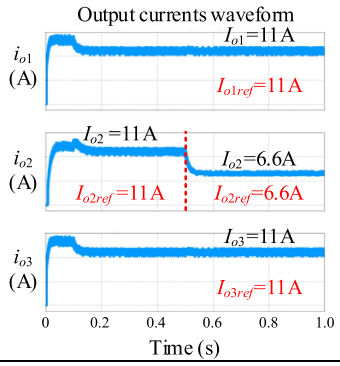	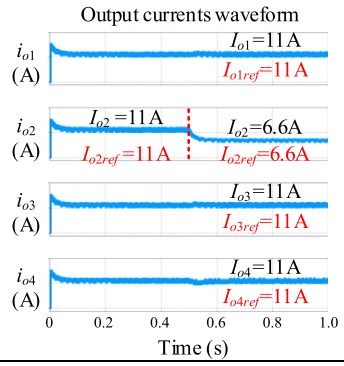

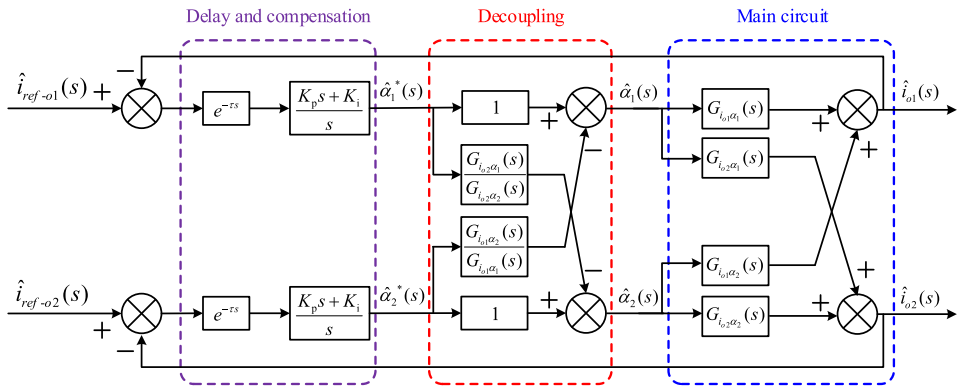

Fig. 6. Control block diagram of the two-module WPT system.

switches, as shown in Fig. 2. For example, the phase difference of the switching signal of S_{11} and S_{21} in Fig. 1(b) is given by

$$\theta_{S_{21}}(t) - \theta_{S_{11}}(t) = \frac{\alpha_1(t) - \alpha_2(t)}{2} + \theta_2(t) - \theta_1(t). \quad (21)$$

C. Stability Analysis of Two-Module WPT System

Based on the small-signal model, the stability of the two-module system is discussed. With the parameters of a two-module WPT system given in Table III, the matrices of the state equations, i.e., $\boldsymbol{A}$, $\boldsymbol{B}$, and $\boldsymbol{C}$, can be calculated. Assuming that the steady-state inverter phase shift angles of the two modules are both 150°, the steady-state operating point can be obtained, as given in Table I.

Based on the control diagram shown in Fig. 5, a simplified control block diagram as shown in Fig. 7(a) can be derived (delay is not considered), in which the variables are all 2-D vectors. The block diagram of the open loop system is given in Fig. 7(b). The transfer function of the compensation network $G_c(s)$, the transfer function matrix of the decoupling matrix $\boldsymbol{G}_{de}(s)$, and the open loop transfer function matrix $\boldsymbol{G}_{\mathrm{WPT}}(s)$ in Fig. 7(a) can be expressed as follows:

$$G_c(s) = \frac{K_p s + K_i}{s}$$

$$\boldsymbol{G}_{de}(s) = \begin{bmatrix} 1 & -\dfrac{G_{i_{o1}\alpha_2}(s)}{G_{i_{o1}\alpha_1}(s)} \\ -\dfrac{G_{i_{o2}\alpha_1}(s)}{G_{i_{o2}\alpha_2}(s)} & 1 \end{bmatrix}$$

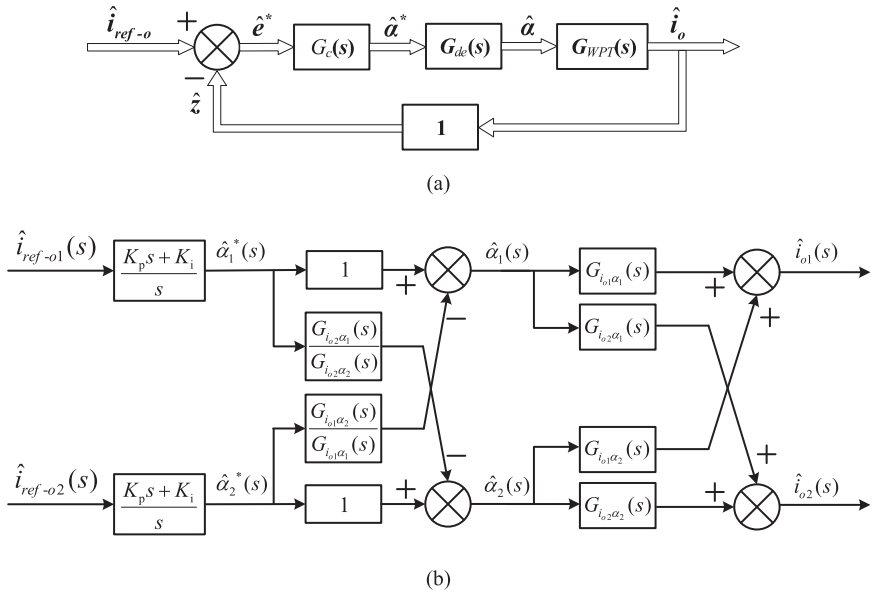

Fig. 7. Block diagram (a) in vector representation and (c) of the open loop system.

TABLE VII
MEASURED PARAMETERS OF THE TWO-MODULE WPT SYSTEM

Parameters	Aligned	100 mm misaligned
R_{AC}	0.217 Ω	0.213 Ω
L_{1T}	326.8 μH	326.9 μH
L_{1R}	338.0 μH	337.8 μH
L_{2T}	332.6 μH	332.3 μH
L_{2R}	333.5 μH	333.1 μH
M_{1T1R}	48.2 μH	36.7 μH
M_{1T2T}	-26.3 μH	-26.0 μH
M_{1T2R}	-11.6 μH	-11.9 μH
M_{2T1R}	-13.0 μH	-5.1 μH
M_{1R2R}	-26.7 μH	-26.3 μH
M_{2T2R}	47.5 μH	36.1 μH
C_{1T}	10.9 nF	10.9 nF
C_{1R}	10.5 nF	10.5 nF
C_{2T}	10.6 nF	10.6 nF
C_{2R}	10.6 nF	10.6 nF

TABLE VIII
ELECTRICAL SPECIFICATIONS OF THE TWO-MODULE WPT SYSTEM

Parameters	Values
Total Output Power	6.9 kW
Input DC Voltage	400 V
Battery Voltage	330 V
Operating Frequency	86.2 kHz

$$\boldsymbol{G}_{\mathrm{WPT}}(s)=\boldsymbol{C}(s\boldsymbol{I}-\boldsymbol{A})^{-1}\boldsymbol{B}_2 \tag{22}$$

where $\boldsymbol{B}_2$ is defined as

$$\boldsymbol{B}_2=\boldsymbol{B}\begin{bmatrix}10\\00\\01\\00\end{bmatrix}.$$

With (22) and Fig. 7(a), we can get

$$\begin{cases}\hat{\boldsymbol{i}}_{\boldsymbol{ref-o}}-\hat{\boldsymbol{z}}=\hat{\boldsymbol{e}}^*\\ G_c(s)\cdot\hat{\boldsymbol{e}}^*=\hat{\boldsymbol{\alpha}}^*\\ \boldsymbol{G}_{de}(s)\cdot\hat{\boldsymbol{\alpha}}^*=\hat{\boldsymbol{\alpha}}\\ \boldsymbol{G}_{\mathrm{WPT}}(s)\cdot\hat{\boldsymbol{\alpha}}=\hat{\boldsymbol{i}}_{\boldsymbol{o}}\\ \hat{\boldsymbol{i}}_{\boldsymbol{o}}=\hat{\boldsymbol{z}}.\end{cases} \tag{23}$$

By solving (23), the open loop and close loop transfer function matrices of $\hat{\boldsymbol{i}}_{\boldsymbol{ref-o}}$ to $\hat{\boldsymbol{i}}_{\boldsymbol{o}}$ can be obtained as

$$\begin{cases}\boldsymbol{G}_{\mathrm{open}}(s)=\boldsymbol{G}_{\mathrm{WPT}}(s)\,\boldsymbol{G}_{de}(s)\,G_c(s)\\ \boldsymbol{G}_{\mathrm{clsd}}(s)=(\boldsymbol{I}+\boldsymbol{G}_{\mathrm{WPT}}(s)\,\boldsymbol{G}_{de}(s)\,G_c(s))^{-1}\\ \qquad\qquad\times\boldsymbol{G}_{\mathrm{WPT}}(s)\,\boldsymbol{G}_{de}(s)\,G_c(s).\end{cases} \tag{24}$$

The characteristic polynomials of $\boldsymbol{G}_{\mathrm{WPT}}(s)$ can be expressed as

$$\rho_{\mathrm{GWPT}}(s)=(\det(s\boldsymbol{I}-\boldsymbol{A}))^2. \tag{25}$$

Thus, the open loop characteristic polynomial $\rho_{\mathrm{open}}(s)$ can be calculated as

$$\rho_{\mathrm{open}}(s)=sG_{i_{o2}\alpha_2}(s)G_{i_{o1}\alpha_1}(s)\cdot(\det(s\boldsymbol{I}-\boldsymbol{A}))^4. \tag{26}$$

The relationship between the open loop characteristic polynomial $\rho_{\mathrm{open}}(s)$ and the close loop characteristic polynomial $\rho_{\mathrm{clsd}}(s)$ can be expressed as [36], [37], [38]

$$\frac{\rho_{\mathrm{clsd}}(s)}{\rho_{\mathrm{open}}(s)}=\det[\boldsymbol{I}+\boldsymbol{G}_{\mathrm{open}}(s)]. \tag{27}$$

Take the following three cases as an example:
1) $K_p=1, K_i=10$;
2) $K_p=0.002, K_i=1000$;
3) $K_p=0.002, K_i=10$.

Consider nonduplicate items in the polynomial, $\rho_{\mathrm{open}}(s)$ has two zeros on the right half-plane in all these three cases. Enlarging the smaller portion of the curves, the Nyquist schematic

TABLE IX
EXPERIMENT RESULTS AT THE ALIGNED POSITION

			Aligned	
			Individual feedback control	Decoupling control
Module output currents and inverter output voltages (I_{o1} and I_{o2} are average values)	t (5s/div) u_1、u_2 (500V/div)	Reference changed at red line	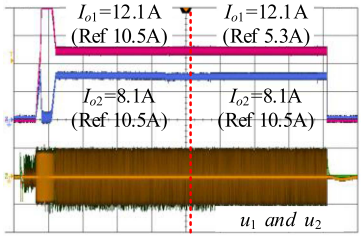	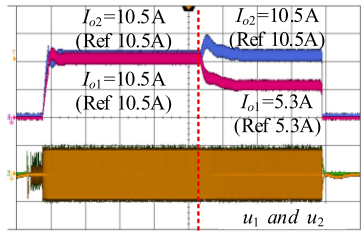
	t (2μs/div) u_1、u_2 (500V/div)	Before changing reference	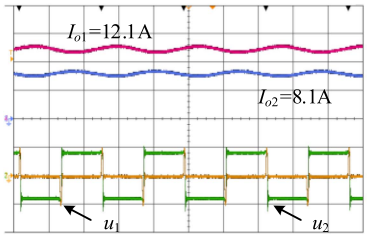	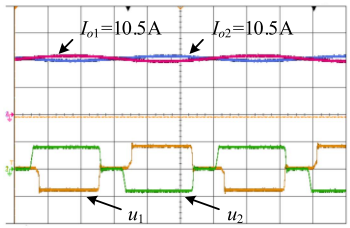
		After changing reference	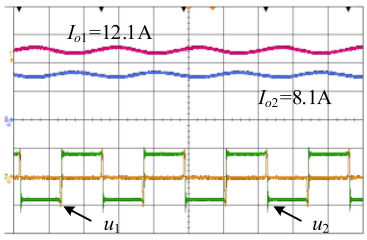	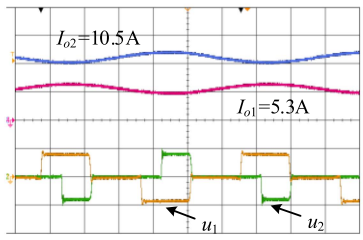
Primary currents and inverter output voltages (I_{T1} and I_{T2} are RMS values)	t (5μs/div) u_1、u_2 (500V/div)	Before changing reference	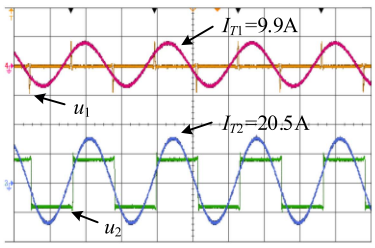	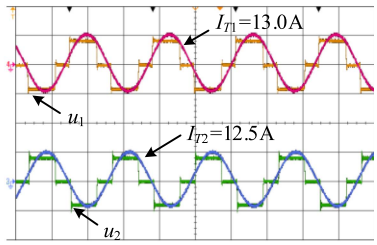
		After changing reference	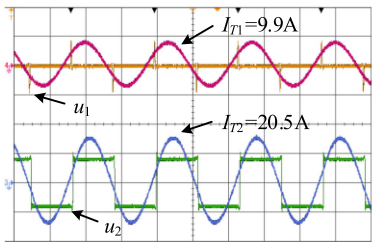	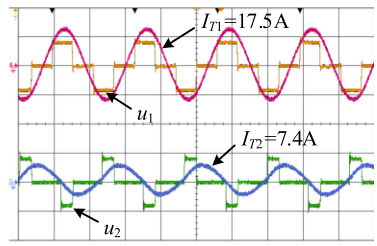

diagrams of the left half-plane in these three cases are shown in Fig. 8. The number of positive crossings minus the number of negative crossings of the three Nyquist curves are 0, 0, and 2, respectively. Therefore, only the last case is stable.

Fig. 9 shows the simulation waveforms corresponding to the above PI parameters. The PI controller in the steady-state simulation has a preset value, which corresponds to the steady-state operating point of Table I. It can be seen that if the system is stable, the output waveform of the corresponding PI controller is stable. If the system is unstable, the output waveform of the PI controller has an oscillation divergence trend. However, since the output of the PI controller and the output of the decoupling stage will be limited, the output currents cannot be increased infinitely. The simulation results are consistent with the theoretical analysis.

In the prototype for experiments, there is a delay caused by wireless communication. In the prototype, the HC05 Bluetooth module is used. According to the measurement results of the Bluetooth module [39], the delay is between 20 and 50 ms. Thus, a delay of 50 ms is included in the stability analysis of

TABLE X
EXPERIMENT RESULTS AT THE MISALIGNED POSITION

			100 mm misaligned	
			Individual feedback control	Decoupling control
Module output currents and inverter output voltages (I_{o1} and I_{o2} are average values)	t (5s/div) u_1、u_2 (500V/div)	Reference changed at red line	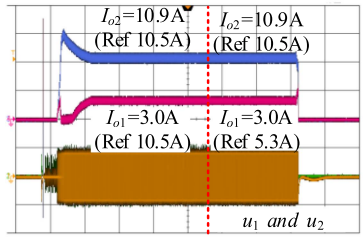	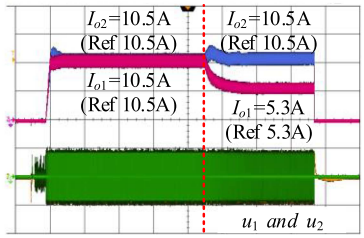
	t (2μs/div) u_1、u_2 (500V/div)	Before changing reference	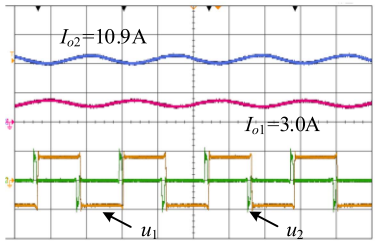	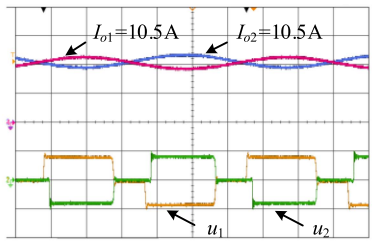
		After changing reference	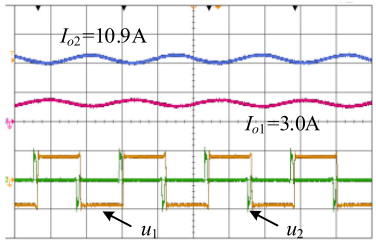	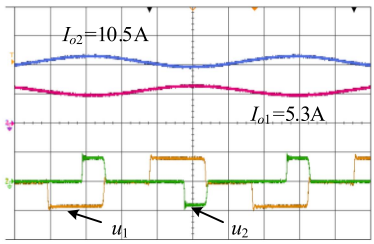
Primary currents and inverter output voltages (I_{T1} and I_{T2} are RMS values)	t (5μs/div) u_1、u_2 (500V/div)	Before changing reference	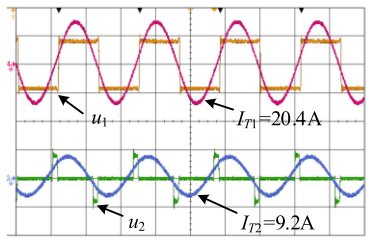	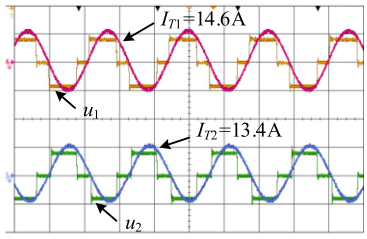
		After changing reference	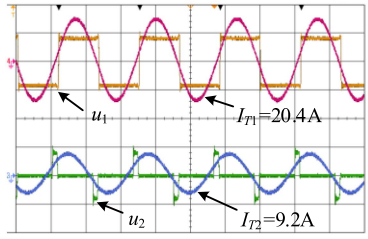	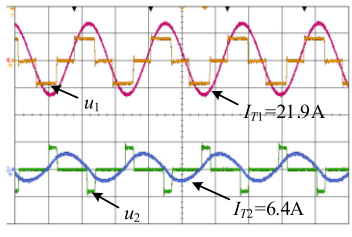

the prototype. To facilitate the calculation, the first-order Pade approximation is adopted [38]

$$e^{-\tau s} = \frac{1 - \frac{\tau}{2}s}{1 + \frac{\tau}{2}s}. \tag{28}$$

The stability analysis is carried out based on the experimental parameters used in Section V as given in Table VII. The compensation network parameters are set as $K_p = 0.02$ and $K_i = 0.002$. Since the delay does not introduce new poles in the right half-plane, $\rho_{\text{open}}(s)$ still has two zeros on the right half-plane. The left half-plane Nyquist diagram of the system is shown in Fig. 10, which indicates the prototype with the said PI parameters is stable.

IV. SIMULATION VERIFICATION

Circuit simulations have been carried out based on two-module, three-module, and four-module WPT systems (see Fig. 11). All windings, with parameters given in Table II, are identical in these three systems. The ac resistances, the inductances, the phase angles of the decoupled input voltages at the

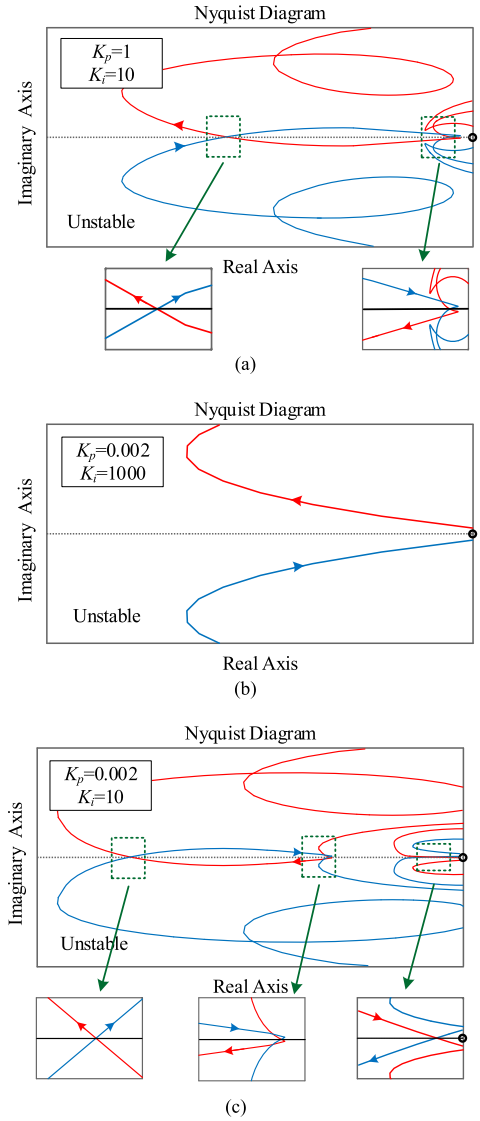

Fig. 8. Left half-plane Nyquist diagrams of det[$\boldsymbol{I}+\boldsymbol{G}_{\mathrm{open}}(s)$] when (a) $K_p = 1$ and $K_i = 10$, (b) $K_p = 0.002$ and $K_i = 1000$, and (c) $K_p = 0.002$ and $K_i = 10$.

aligned position, and the PI parameters are given in Tables III–V. The ac resistances are calculated using the method described in [40]. The circuit model used in the simulations is the same as that given in Fig. 1(b). The battery voltage is set at 330 V. The operating frequency equals to the resonant frequency of the resonators, which is 85 kHz.

Simulation results are shown in Table VI. Initially, the reference output currents of all modules are set at 11 A. Then, at $t = 0.5$ s, Module 2 changes its output current reference to 6.6 A, whereas the other module(s) maintain the same. Using conventional negative-feedback control for each module, all three systems fail to follow the reference values in one or more modules. By contrast, the proposed decoupling control is able to follow the reference values in all the modules of the three systems. The PI parameters maintain the same for the two control methods.

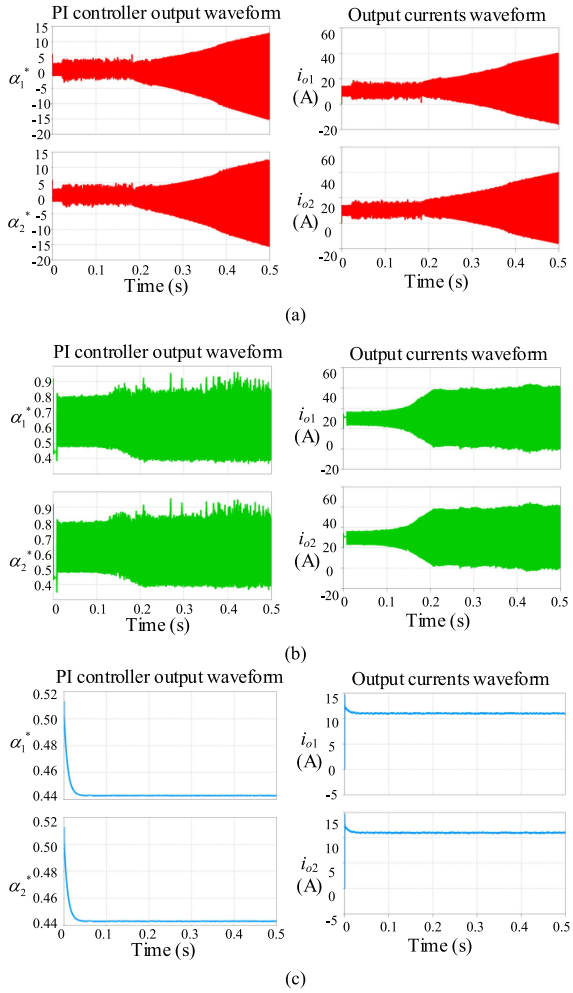

Fig. 9. Simulation waveforms when (a) $K_p = 1$ and $K_i = 10$, (b) $K_p = 0.002$ and $K_i = 1000$, and (c) $K_p = 0.002$ and $K_i = 10$.

V. Experimental Verification

A. Setup for Experiments

A two-module WPT prototype is built for experiments, as shown in Fig. 12. The geometric parameters of the windings are the same as those given in Table II. The measured parameters of the couplers and capacitors in the aligned position and the position with 100 mm horizontal misalignment are given in Table VII. The misalignment direction is shown in Fig. 12(a). The electrical specifications of the prototype are shown in Table VIII. The compensation network parameters are set as $K_p = 0.02$ and $K_i = 0.002$, respectively. The inverters and the rectifiers are developed using MOSFET C2M0025120D and the ultrafast diode RURG80100, respectively. The primary-secondary communication is realized with the Bluetooth module HC05.

B. Results and Discussion

The experimental results of using two control methods, i.e., the proposed decoupling control and the conventional negative-feedback control, are given in Tables IX and X. In the case of using the conventional negative-feedback control for each

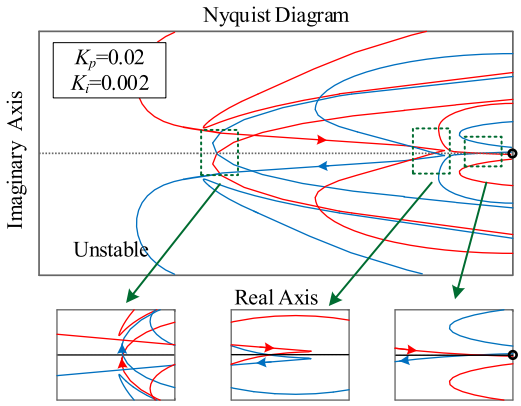

Fig. 10. Left half-plane Nyquist diagram of the prototype system.

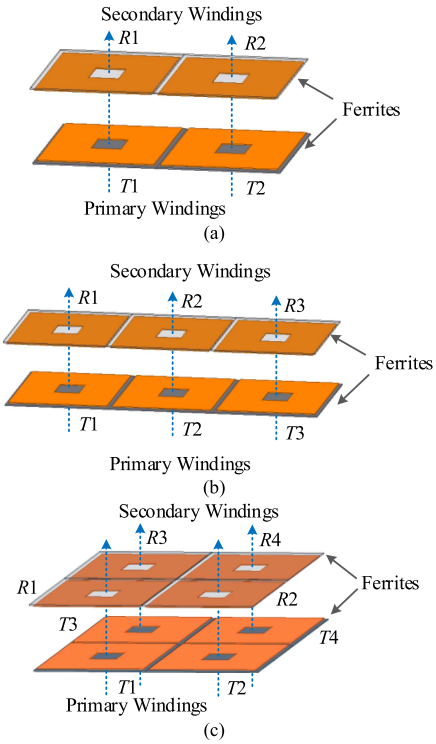

Fig. 11. Couplers of (a) two-module system, (b) three-module system, and (c) four-module system.

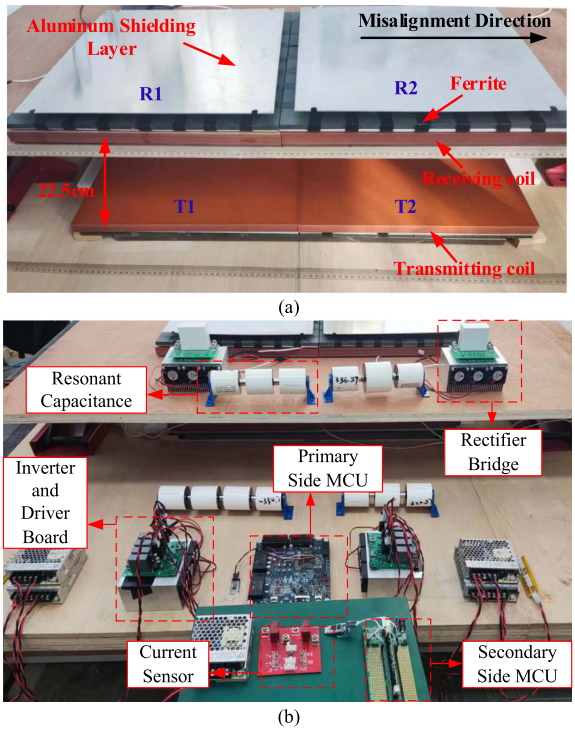

Fig. 12. Experimental prototype. (a) Couplers. (b) Aerial view of the whole system.

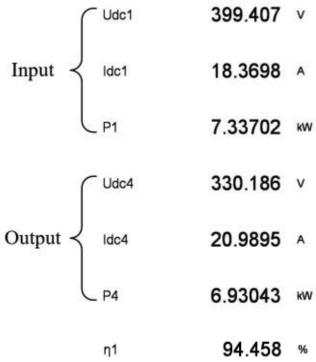

Fig. 13. Captured DC–DC efficiency at 6.9 kW from power analyzer.

module, the output currents cannot follow the reference values. For example, at the aligned position, when the references for I_{o1} and I_{o2} are both 10.5 A, the actual I_{o1} and I_{o2} finally reach 12.1 A and 8.1 A, respectively. Under this condition, the PI controller of Module 1 should decrease the input voltage of Module 1 and that of Module 2 should increase the input voltage of Module 2. However, at this moment, the input voltage of Module 1 has been reduced to nearly zero and that of Module 2 has been increased to the maximum. This indicates that the outputs of the PI controllers have been divergent, which is caused by the nonidentical parameters of two modules and the effect of the strong cross couplings between modules. Because of the divergence, the changes in the reference value do not affect the controller outputs, and thereby the output currents of the two modules maintain the same after changing the reference values. Therefore, it is obvious that the individual negative-feedback control is not able to separately regulate I_{o1} and I_{o2} under this situation. Similar results are observed in the other scenarios when using the individual negative-feedback control. By contrast, after applying the proposed decoupling control, the output currents of the two modules follow the reference values well, regardless of whether the windings are aligned or not. This is consistent with the stability analysis given in Section III-C.

The measured dc–dc efficiency at 6.9 kW is 94.5% as shown in Fig. 13. The loss breakdown is given in Fig. 14. The parameters and formulas used for loss calculation are given in the Appendix.

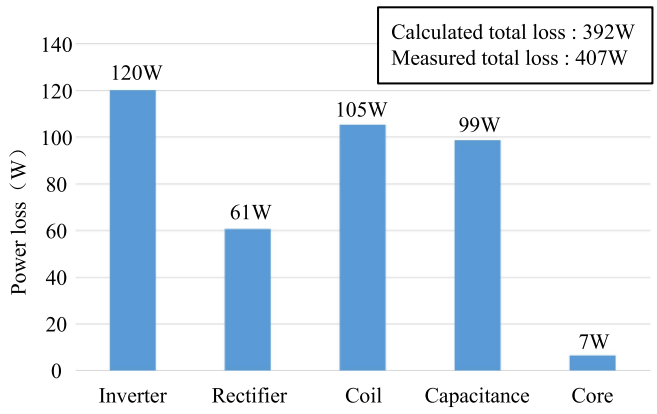

Fig. 14. Calculated DC–DC loss breakdown at 6.9 kW.

VI. Conclusion

The concept of modular WPT is a promising approach to increasing the power level of WPT systems. However, modular WPT systems encounter a critical challenge different from other power electronics systems, which is the interferences caused by the cross couplings among different modules. Applying the conventional negative-feedback control individually to each module might not be able to achieve the desired output. This article derives the small-signal model of the two-module WPT system and proposes a corresponding decoupling control method. According to the transfer function of the main circuit, the influences caused by cross couplings can be eliminated by including an extra decoupling component in the input voltage of each module. Thereby, independent control for each module is successfully realized, which means the output of one module can be changed without affecting the outputs of the other modules. This control method can be extended to an *n*-module WPT system. With the decoupling control method, the overall control block diagram is established and the stability of the closed-loop system is theoretically analyzed. The decoupling control is verified by simulations on two-module, three-module, and four-module WPT systems. Eventually, a 7 kW two-module WPT prototype is built. The experimental result proves that the proposed decoupling control method can realize individual output control for each module. The measured dc–dc efficiency of the prototype is 94.5%.

Appendix

Parameters for loss calculation are given in Table XI. Coil resistances can be calculated by the method introduced in [40]. The core loss is obtained through FEA software.

The loss of the capacitors and the coils can be directly calculated with the ac resistances. The conduction loss of each diode is given by

$$P_{rec} = \frac{1}{2} I_o V_D + \frac{1}{2} I_o^2 r_0. \tag{A1}$$

According to the inverter waveform in Fig. 6 and considering the dead time, the calculation formulas of the turn-ON loss, the turn-OFF loss, the MOSFET conduction loss, the antiparallel diode conduction loss, and the antiparallel diode reverse recovery loss of S_1 are given, respectively, by [41]

$$P_{\mathrm{ON\_S11}} = f * E_{\mathrm{ON}} \tag{A2}$$

$$P_{\mathrm{OFF\_S11}} = f * E_{\mathrm{OFF}} \tag{A3}$$

$$\theta_{\mathrm{dead}} = \pi f t_{\mathrm{dead}} \tag{A4}$$

$$P_{\mathrm{MOS\_S11}} = \left[\frac{1}{2\pi} \int_{\theta_{S_1}}^{\theta_{S_1}+\pi-\theta_{\mathrm{dead}}} \left(\sqrt{2} I_{1T} \sin(\theta) \right)^2 d\theta \right] R_{\mathrm{ON}} \tag{A5}$$

$$P_{\mathrm{diode\_S11}} = \left[\frac{1}{2\pi} \int_{\theta_{S_1}+\pi-\theta_{\mathrm{dead}}}^{\theta_{S_1}+\pi} \sqrt{2} I_{1T} \sin(\theta) d\theta \right] V_{\mathrm{DM}} \tag{A6}$$

$$P_{\mathrm{res}} = \frac{1}{2} Q_{rr} V_{\mathrm{DM}} \tag{A7}$$

where θ_{dead} represents the angle corresponding to dead time, f is the experimental operating frequency, and I_{T1} is the RMS value of the primary current of Module 1.

TABLE XI
Parameters for Loss Calculation

Parameters	Values
The primary coil R_{AC}	0.189 Ω
The secondary coil R_{AC}	0.188 Ω
Capacitance resistance @Q=1000	0.177 Ω
Core loss	6.5 W
Diode V_D	0.8 V
Diode r_0	50 mΩ
MOS R_{ON}	25 mΩ
MOS E_{on} @400V,5A	0.17 mJ
MOS E_{off} @400V,5A	0.07 mJ
MOS E_{off} @400V,13A	0.12 mJ
Reverse Recovery Charge Q_{rr}	406 nC
Anti-parallel Diode V_{DM}	3.3 V
The dead time t_{dead}	500ns

References

[1] G. A. Covic and J. T. Boys, "Inductive power transfer," *Proc. IEEE*, vol. 101, no. 6, pp. 1276–1289, Jun. 2013.
[2] S. Li and C. C. Mi, "Wireless power transfer for electric vehicle applications," *IEEE J. Emerg. Sel. Topics Power Electron.*, vol. 3, no. 1, pp. 4–17, Mar. 2015.
[3] R. Bosshard and J. W. Kolar, "Multi-objective optimization of 50 kW/85 kHz IPT system for public transport," *IEEE J. Emerg. Sel. Topics Power Electron.*, vol. 4, no. 4, pp. 1370–1382, Dec. 2016.
[4] R. Bosshard, U. Iruretagoyena, and J. W. Kolar, "Comprehensive evaluation of rectangular and double-D coil geometry for 50 kW/85 kHz IPT system," *IEEE J. Emerg. Sel. Topics Power Electron.*, vol. 4, no. 4, pp. 1406–1415, Dec. 2016.
[5] J. Pries, V. P. N. Galigekere, O. C. Onar, and G. Su, "A 50-kW three-phase wireless power transfer system using bipolar windings and series resonant networks for rotating magnetic fields," *IEEE Trans. Power Electron.*, vol. 35, no. 5, pp. 4500–4517, May 2020.
[6] V. P. Galigekere et al., "Design and implementation of an optimized 100 kW stationary wireless charging system for EV battery recharging," in *Proc. IEEE Energy Convers. Congr. Expo.*, 2018, pp. 3587–3592.
[7] C. R. Sullivan, "Optimal choice for number of strands in a litz-wire transformer winding," *IEEE Trans. Power Electron.*, vol. 14, no. 2, pp. 283–291, Mar. 1999, doi: 10.1109/63.750181.
[8] A. U. Ibrahim, W. Zhong, and D. M. Xu, "A 50 kW modular wireless power transfer system with low stray magnetic field," *IEEE Trans. Power Electron.*, vol. 36, no. 9, pp. 9941–9954, Sep. 2021, doi: 10.1109/TPEL.2021.3064373.

[9] T. Shijo, K. Ogawa, M. Suzuki, Y. Kanekiyo, M. Ishida, and S. Obayashi, "EMI reduction technology in 85 kHz band 44 kW wireless power transfer system for rapid contactless charging of electric bus," in *Proc. IEEE Energy Convers. Congr. Expo.*, 2016, pp. 1–6.
[10] Y. Li et al., "A novel WPT system based on dual transmitters and dual receivers for high power applications: Analysis, design and implementation," *Energies*, vol. 10, no. 2, 2017, Art. no. 174.
[11] J. Gao, "Traveling magnetic field for homogeneous wireless power transmission," *IEEE Trans. Power Del.*, vol. 22, no. 1, pp. 507–514, Jan. 2007.
[12] G. A. Covic, J. T. Boys, M. L. G. Kissin, and H. G. Lu, "A three-phase inductive power transfer system for roadway-powered vehicles," *IEEE Trans. Ind. Electron.*, vol. 54, no. 6, pp. 3370–3378, Dec. 2007.
[13] H. Matsumoto, Y. Neba, K. Ishizaka, and R. Itoh, "Model for a three-phase contactless power transfer system," *IEEE Trans. Power Electron.*, vol. 26, no. 9, pp. 2676–2687, Sep. 2011.
[14] D. J. Thrimawithana and U. K. Madawala, "A three-phase bi-directional IPT system for contactless charging of electric vehicles," in *Proc. IEEE Int. Symp. Ind. Electron.*, 2011, pp. 1957–1962.
[15] W. M. Ng, C. Zhang, D. Lin, and S. Y. R. Hui, "Two- and three-dimensional omnidirectional wireless power transfer," *IEEE Trans. Power Electron.*, vol. 29, no. 9, pp. 4470–4474, Sep. 2014.
[16] H. Matsumoto, Y. Neba, H. Iura, D. Tsutsumi, K. Ishizaka, and R. Itoh, "Trifoliate three-phase contactless power transformer in case of winding-alignment," *IEEE Trans. Ind. Electron.*, vol. 61, no. 1, pp. 53–62, Jan. 2014.
[17] A. Abdolkhani, A. P. Hu, and J. Tian, "Autonomous polyphase current-fed push–pull resonant converter based on ring coupled oscillators," *IEEE J. Emerg. Sel. Topics Power Electron.*, vol. 3, no. 2, pp. 568–576, Jun. 2015.
[18] M. L. G. Kissin, J. T. Boys, and G. A. Covic, "Interphase mutual inductance in polyphase inductive power transfer systems," *IEEE Trans. Ind. Electron.*, vol. 56, no. 7, pp. 2393–2400, Jul. 2009.
[19] Y. Song, U. K. Madawala, T. Duleepa J, and A. P. Hu, "Cross-coupling effects of poly-phase bi-directional inductive power transfer systems used for EV charging," in *Proc. IEEE 2nd Int. Future Energy Electron. Conf.*, 2015, pp. 1–7.
[20] A. Zaheer, G. A. Covic, and D. Kacprzak, "A bipolar pad in a 10-kHz 300-W distributed IPT system for AGV applications," *IEEE Trans. Ind. Electron.*, vol. 61, no. 7, pp. 3288–3301, Jul. 2014, doi: 10.1109/TIE.2013.2281167.
[21] S. Kim, G. A. Covic, and J. T. Boys, "Tripolar pad for inductive power transfer systems for EV charging," *IEEE Trans. Power Electron.*, vol. 32, no. 7, pp. 5045–5057, Jul. 2017.
[22] Y. Liu, R. Mai, D. Liu, Y. Li, and Z. He, "Efficiency optimization for wireless dynamic charging system with overlapped DD coil arrays," *IEEE Trans. Power Electron.*, vol. 33, no. 4, pp. 2832–2846, Apr. 2018, doi: 10.1109/TPEL.2017.2751593.
[23] J. Pries, V. P. N. Galigekere, O. C. Onar, and G. Su, "A 50-kW three-phase wireless power transfer system using bipolar windings and series resonant networks for rotating magnetic fields," *IEEE Trans. Power Electron.*, vol. 35, no. 5, pp. 4500–4517, May 2020, doi: 10.1109/TPEL.2019.2942065.
[24] Y. Li, T. Lin, R. Mai, L. Huang, and Z. He, "Compact double-sided decoupled coils-based WPT systems for high-power applications: Analysis, design, and experimental verification," *IEEE Trans. Transp. Electrific.*, vol. 4, no. 1, pp. 64–75, Mar. 2018, doi: 10.1109/TTE.2017.2745681.
[25] Y. Li et al., "A new coil structure and its optimization design with constant output voltage and constant output current for electric vehicle dynamic wireless charging," *IEEE Trans. Ind. Inform.*, vol. 15, no. 9, pp. 5244–5256, Sep. 2019, doi: 10.1109/TII.2019.2896358.
[26] R. Mai, Y. Luo, B. Yang, Y. Song, S. Liu, and Z. He, "Decoupling circuit for automated guided vehicles IPT charging systems with dual receivers," *IEEE Trans. Power Electron.*, vol. 35, no. 7, pp. 6652–6657, Jul. 2020, doi: 10.1109/TPEL.2019.2955970.
[27] H. Matsumoto, Y. Neba, K. Ishizaka, and R. Itoh, "Model for a three-phase contactless power transfer system," *IEEE Trans. Power Electron.*, vol. 26, no. 9, pp. 2676–2687, Sep. 2011, doi: 10.1109/TPEL.2011.2124472.
[28] Y. Li, R. Mai, L. Lu, T. Lin, Y. Liu, and Z. He, "Analysis and transmitter currents decomposition based control for multiple overlapped transmitters based WPT systems considering cross couplings," *IEEE Trans. Power Electron.*, vol. 33, no. 2, pp. 1829–1842, Feb. 2018, doi: 10.1109/TPEL.2017.2690061.
[29] B. Bahrani, A. Karimi, B. Rey, and A. Rufer, "Decoupled dq-current control of grid-tied voltage source converters using nonparametric models," *IEEE Trans. Ind. Electron.*, vol. 60, no. 4, pp. 1356–1366, Apr. 2013, doi: 10.1109/TIE.2012.2185017.
[30] N. Weise, "DQ current control of a bidirectional, isolated, single-stage ac-dc converter for vehicle-to-grid applications," in *Proc. IEEE Power Energy Soc. Gen. Meeting*, 2013, pp. 1–5, doi: 10.1109/PESMG.2013.6672847.
[31] S. R. Sanders, J. M. Noworolski, X. Z. Liu, and G. C. Verghese, "Generalized averaging method for power conversion circuits," *IEEE Trans. Power Electron.*, vol. 6, no. 2, pp. 251–259, Apr. 1991, doi: 10.1109/63.76811.
[32] T. Tan, K. Chen, Y. Jiang, Q. Lin, L. Yuan, and Z. Zhao, "A bidirectional wireless power transfer system control strategy independent of real-time wireless communication," *IEEE Trans. Ind. Appl.*, vol. 56, no. 2, pp. 1587–1598, Mar./Apr. 2020, doi: 10.1109/TIA.2019.2961311.
[33] E. X.-Q. Yang, "Extended describing function method for small-signal modeling of resonant and multi-resonant converters," Ph.D. dissertation, Dept. Elect. Eng., Virginia Tech, Blacksburg, VA, USA, 1994.
[34] L. A. Garcia-Rodriguez, C. Deng, J. C. Balda, and A. Escobar-Mejía, "Analysis, modeling and control of an interleaved isolated boost series resonant converter for microinverter applications," in *Proc. IEEE Appl. Power Electron. Conf. Expo.*, 2016, pp. 362–369, doi: 10.1109/APEC.2016.7467898.
[35] N. Mohan, T. M. Undeland, and W. P. Robbins, *Power Electronics: Converters, Applications, and Design*. New York, NY, USA: Wiley, 1995.
[36] G. Fusco and M. Russo, "Robust MIMO design of decentralized voltage controllers of PV systems in distribution networks," *IEEE Trans. Ind. Electron.*, vol. 64, no. 6, pp. 4610–4620, Jun. 2017, doi: 10.1109/TIE.2017.2652386.
[37] H. Zhang, L. Harnefors, X. Wang, H. Gong, and J. -P. Hasler, "Stability analysis of grid-connected voltage-source converters using SISO modeling," *IEEE Trans. Power Electron.*, vol. 34, no. 8, pp. 8104–8117, Aug. 2019, doi: 10.1109/TPEL.2018.2878930.
[38] K. Ogata, *Discrete-Time Control Systems*, 2nd ed. Hoboken, NJ, USA: Prentice-Hall, 1995.
[39] M. Faiqurahman, D. A. Novitasari, and Z. Sari, "QoS analysis of kinematic effects for bluetooth hc-05 and NRF24L01 communication modules on WBAN system," *Kinetik Game Technol. Inf. Syst. Comput. Netw. Comput. Electron. Control*, May 2019.
[40] J. Mühlethaler, "Modeling and multi-objective optimization of inductive power components," Ph.D. dissertation, Dept. Elect. Eng., ETH Zurich, Switzerland, 2012.
[41] N. He, M. Chen, J. Wu, N. Zhu, and D. Xu, "20-kW zero-voltage-switching SiC-MOSFET grid inverter with 300 kHz switching frequency," *IEEE Trans. Power Electron.*, vol. 34, no. 6, pp. 5175–5190, Jun. 2019, doi: 10.1109/TPEL.2018.2866824.

Chen Zhu (Student Member, IEEE) received the B.S. degree in electrical engineering from the Beijing University of Aeronautics and Astronautics, Beijing, China, in 2018. He is currently working toward the Ph.D. degree in power electronics with the College of Electrical Engineering, Zhejiang University, Hangzhou, China.

His current research interests include wireless power transfer technologies and power electronics.

Wenxing Zhong (Senior Member, IEEE) received the B.Eng. degree in electrical engineering from Tsinghua University, Beijing, China, in 2007, and the Ph.D. degree in power electronics from the City University of Hong Kong, Hong Kong, in 2012.

He is currently a Professor with the Department of Electrical Engineering, Zhejiang University, Hangzhou, China. From 2016 to 2017, he was a Research Assistant Professor with the Department of Electrical and Electronic Engineering, The University of Hong Kong, Hong Kong. His research interests include wireless power transfer and power electronics.

Prof. Zhong was the recipient of two transactions first prize paper awards from IEEE Power Electronics Society.